Progress In Electromagnetics Research C, Vol. 147, 45-53, 2024

(Received 24 May 2024, Accepted 4 August 2024, Scheduled 23 August 2024)

Design and Electromagnetic Performance Investigation of a Compact Pneumatic Drive Linear Generator Used in Wave Energy Conversion

Yusheng Hu*, Chouwei Guo, Mengyuan Niu, and Lijin He

The College of Marine Equipment and Mechanical Engineering, Jimei University, Xiamen 361021, China

ABSTRACT: Ocean wave energy is an inexhaustible clean new energy resource, and wave direct-drive linear generator is an energy converter receiving wide attention, but it suffers from the deficiencies of difficult energy harvesting, slow movement speed, large size, and small power generation, etc., so there is an urgent requirement to develop high-efficiency small-scale energy conversion devices. In this paper, a Pneumatic Drive Linear Generator (PDLG) is provided as a high efficient compact wave energy converter (WEC). The structure design and automatic reciprocating control system for the PDLG are implemented. The field distribution characteristics and parameters effects are analyzed using the finite-element method based on scalar magnetic potential. Finally, a prototype was fabricated to verify the performance of the PDLG. The experimental results are in good agreement with that of the theoretical prediction. The results of the study show that the provided PDLG can meet the requirements of high efficient wave energy harvesting, compact structure, and larger power generation.

1. INTRODUCTION

A considerable amount of research work has been carried out on the exploitation and utilization of the ocean wave energy. An interface is usually needed to convert the mechanical energy of wave motion into electric energy. The interface is generally called power take-off (PTO) system, whose roles are smoothing the non-steady mechanical energy and turning low speed mechanical motion into high speed motion of generator. PTO usually takes the following forms such as hydraulic system, pneumatic system, and gearbox. In general, the output end of the PTO is connected to a rotary generator. However, a complicated driven system is usually required for the rotary generator. In particular, the ocean is a unstructured environment, where driving the rotary generator to operate in a stable manner is very difficult. Therefore, high efficient wave energy converter (WEC) is in demand.

In the past twenty years, direct-drive permanent magnetic linear generator (PMLG) has become an attractive WEC. The body of the direct-drive PMLG is usually anchored under the sea, with its mover connected directly to a float on the sea surface. Of course, by means of certain mechanisms the PMLG can also work by floating on the surface of the sea [1–3]. The direct-drive linear generator operates through straight reciprocating motion, so the driven system is simplified. Especially, the crankshaft is wholly eliminated, and as a result, the loss is reduced. In addition, the cascade structure of linear generators makes the system compact and convenient for installation. The linear generator can operate at higher speed since it avoids the problem of high centrifugal force from rotary generator. Archimedes wave swing (AWS) [4, 5] is an earlier version of a direct-drive wave energy conversion system. In AWS, the linear generator is placed in a compressed air chamber, which is fixed to the seabed, and the mover is connected to a float. Since the AWS system is fully immersed in the sea, it is more robust against storms. Flat type is a fundamental form of linear generators. Flat type linear generators use surface-mounted sheet magnets, which are easy to manufacture and install. In a flat linear generator, air-cored winding is sandwiched between two iron-cored PM translators, as described in [6, 7]. In [8], a core generator (C-GEN) was provided which is a double sided air-cored PM generator. The disadvantage of the flat type linear generator is the existence of transverse end effect.

Tubular structure [9–14] is a more attractive topology of PMLG, since it has no ending flux leakage, cancels out radial forces, and has a highly compact mechanical structure, high efficiency, and better robustness. An iron-cored PMLG can produce larger magnetic flux density but has heavier weight and cogging force, so air-cored PMLG type is widely used. In tubular linear generator, axial-magnetized magnets are more preferred, since radial-magnetized ring magnets are difficult to manufacture.

In conventional PMLG, only a part of the coils or magnets are used, hence transverse-flux permanent magnetic (TFPM) linear generator [6, 15, 16] is recommended to enhance its performance, in which both the coils and magnets are in the stator and the translator consisting of only iron. Other methods have also been proposed, such as Halbach permanent-magnet arrays [2], superconductor coil [17], spiral mover or stator [15], and dual-port [18].

---

* Corresponding author: Yusheng Hu (hysmk@sina.com).

doi:10.2528/PIERC24052404

Published by THE ELECTROMAGNETIC ACADEMY

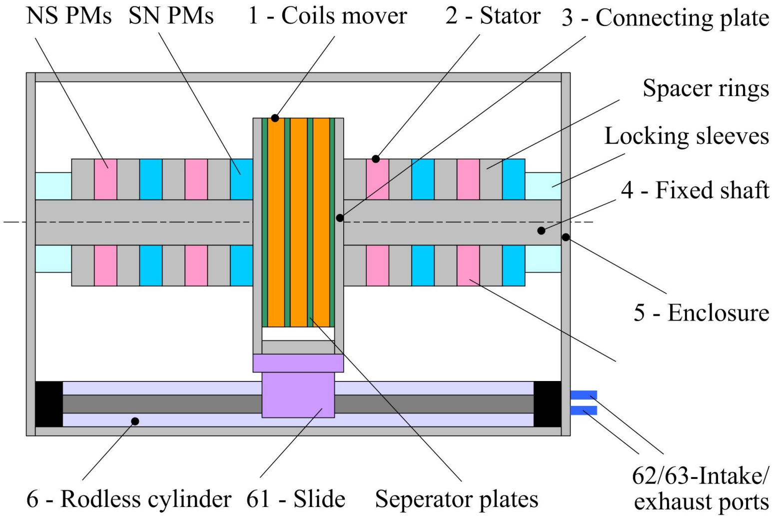

FIGURE 1. Basic structure of the pneumatic drive linear generator.

Although numerous PMLG topologies have been proposed, due to the slow motion of the ocean wave, the size of linear generators is usually very large, which is rather expensive and not applicable to the situation of small or medium waves. Furthermore, since the motion of the wave is irregular, the energy harvesting is very difficult, hence more efficient solutions are needed. The purpose of this paper is to propose a miniaturized Pneumatic Drive Linear Generator (PDLG) for wave energy conversion, whose advantages are that on one hand the generator can greatly increase the operating speed of the mover and thus increase the generating power, and on the other hand, the generator is based on a flexible energy harvesting device for converting wave energy into pneumatic energy, which is more suitable to ocean wave than the rigid energy harvesting device used in the direct-drive PMLGs. The system design of the PDLG is carried out, and its power generation performance is evaluated. The structure of the paper is organized as follows. In Section 2 and Section 3, the structure design and its automatic reciprocating movement control system for the PDLG are described, respectively. The scalar magnetic potential finite-element algorithm is introduced in Section 4. In Sections 5 and 6, the numerical and experimental results are provided, respectively.

2. STRUCTURE DESIGN OF THE PNEUMATIC DRIVE TUBULAR LINEAR GENERATOR

The structure of the PDLG is shown in Fig. 1, which mainly consists of coils mover 1, permanent magnets stator 2, connecting plate 3, fixed shaft 4, enclosure 5, and rodless cylinder 6. The coils mover 1 is rigidly connected to slide 61 through the connection plate 3. External high pressure air is supplied through intake/exhaust ports 62/63 to drive the slide 61 of the rodless cylinder and coils mover 1 to make reciprocating movements, and the coils mover passes through the permanent magnets, thereby voltage is induced.

The stator is assembled from a number of rare-earth ring permanent magnets (PMs) isolated by spacer rings. Instead of iron, non-metallic material, such as plastic, nylon, or Teflon, is used for spacer rings. The PMs are mounted on a hollow shaft whose material is non-magnetic, such as aluminum or stainless steel, to avoid the attractive force from magnets. The PMs are axially magnetized, and the magnetic poles of the PMs are alternately arranged on the shaft, for example, NS, SN, NS, and so on, here, NS PM indicates that the left and right of PM are the North and South poles, respectively. This configuration makes the same polarity between two adjacent magnets and forms radial magnetic poles between magnets, whose North and South poles are varied alternatively in axial direction.

The mover is an assembly of coils surrounding the stator. The length of the mover is much shorter than the stator. The coils are air-cored and fixed in a coils holder and isolated from each other by separator plates. The wires of coils are wound on a insulation tube, which is selected here as a standardized size acrylic tube for convenience. The coils holder is fastened to the slide over the rodless cylinder, and the slide is driven by the rodless cylinder. Therefore, when the cylinder operates it will drive the mover to make reciprocating linear motion.

Compared with the previous wave energy conversion linear generators, the significant features of the proposed PDLG are that the pneumatic drive is favorable to increase the speed of the mover, which greatly improves the power generation, and especially, the use of rodless cylinder makes the structure very compact. In addition, the pneumatic drive is pollution free, low cost, lightweight, easy to control, and no complex mechanical drive is required. Finally, the PDLG provides useful guidance for the development of efficient energy conversion devices for wave energy to air pressure energy, because both gas and seawater are flexible fluids, so the energy storage method of converting wave energy to air pressure energy has a natural advantage.

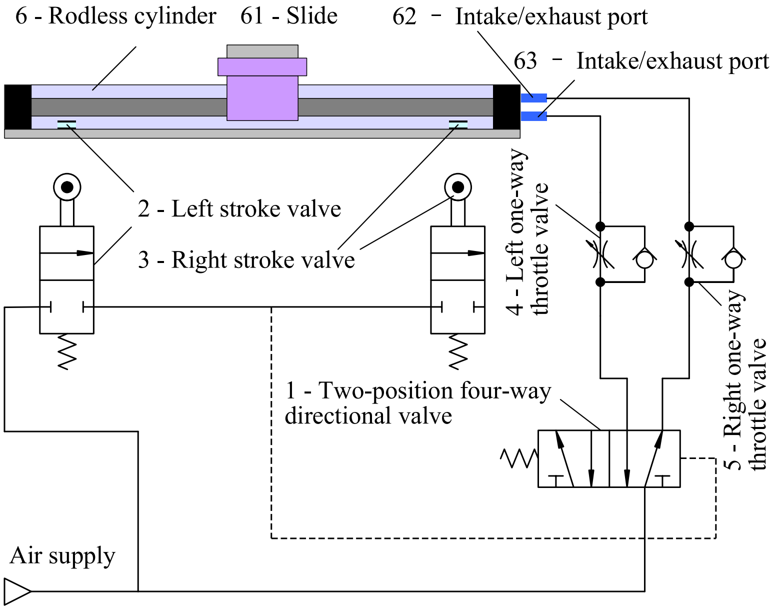

FIGURE 2. Pneumatic control System of reciprocating motion.

3. PNEUMATIC CONTROL SYSTEM OF AUTOMATIC RECIPROCATING MOTION FOR THE MOVER

The automatic reciprocating motion of the coils can be easily realized by several pneumatic valves. The schematic diagram of the pneumatic control system is shown in Fig. 2. The control system comprises two-position four-way directional valve 1, left stroke valve 2, right stroke valve 3, left one-way throttle valve 4, right one-way throttle valve 5, and a mechanical rodless cylinder 6. The rodless cylinder 6 further comprises slide 61, intake/exhaust port 62, intake/exhaust port 63, etc. The working process of the pneumatic control is described as follows.

First of all, the high-pressure air flows from the air supply to the right position of the two-position four-way directional valve 1, and then reaches the right chamber of the rodless cylinder 6 through the right one-way throttle valve 5 and intake/exhaust port 62. Meanwhile, the low-pressure air in the left chamber of the rodless cylinder 6 reaches the left position of the directional valve 1 through the intake/exhaust port 63 and the left one-way throttle valve 4, and finally reaches the exhaust hole. At this stage, the piston of cylinder 6 drives the slide 61 to move to the left.

When the slide 61 touches the left stroke valve 2, the high-pressure air from the air supply will pass through the left stroke valve 2 to the control port of the directional valve 1, and then compels the directional valve 1 to change direction. At this time, the high-pressure air flows from the air supply to the left position of the directional valve 1, then passes through the left throttle valve 4 and intake/exhaust port 63, eventually to the left chamber of the rodless cylinder 6. The air pressure in the left chamber of the cylinder 6 is greater than that in the right chamber, which in turn moves the piston as well as slide 61 to the right. The low-pressure air in the right chamber of the cylinder 1 then passes through the intake/exhaust port 62, the right one-way throttle valve 5, and then the left position of direction valve 1, finally reaches the exhaust hole. This is the process of the slide 61 moving to the right.

When the slide 61 triggers the right stroke valve 3, the air locked in pneumatic control port of the direction valve 1 is discharged through the right stroke valve 3. At this time, the directional valve 1 resets under the action of the spring force, so that the right position of the directional valve 1 works, and the high-pressure air will flow from the air supply to the right position of directional valve 1, and then reaches the right throttle valve 5 and intake/exhaust port 62, finally reaches the right chamber of the cylinder 1. The air pressure at the right end of the piston is greater than that of the left end, which in turn moves the piston and slide 61 of the cylinder 1 to the left.

Repeating the above stages, the reciprocating movement automatic control of the moving coils is realized.

4. FEM ALGORITHM BASED ON SCALAR MAGNETIC POTENTIAL

The electromagnetic field analysis of a linear generator belongs to static magnetic field problem, which can be solved using scalar or vector potential algorithm. For the permanent magnets issue, scalar potential algorithm is more applicable due to its simplicity just like the electric potential in static electric field. Most of the literatures use the vector magnetic potential Finite Element Method (FEM) or analytical method to analyze the electromagnetic field of PMLGs [19–22]. Here, the FEM method based on scalar magnetic potential is described as follows.

According to the electromagnetic field theory [23], the distribution of the scalar magnetic potential φ_{m} in the region where there is no current satisfies the following Laplace's equation

$$\mu_{\mathrm{r}} \nabla^2 \varphi_{\mathrm{m}} = 0 \tag{1}$$

where μ_{r} is the relative permeability of the medium.

The tubular linear generator takes the form of axially symmetric structure, so only a meridian plane needs to be calculated; therefore, the model can be simplified as a two-dimensional (2-D) problem as shown in Fig. 3.

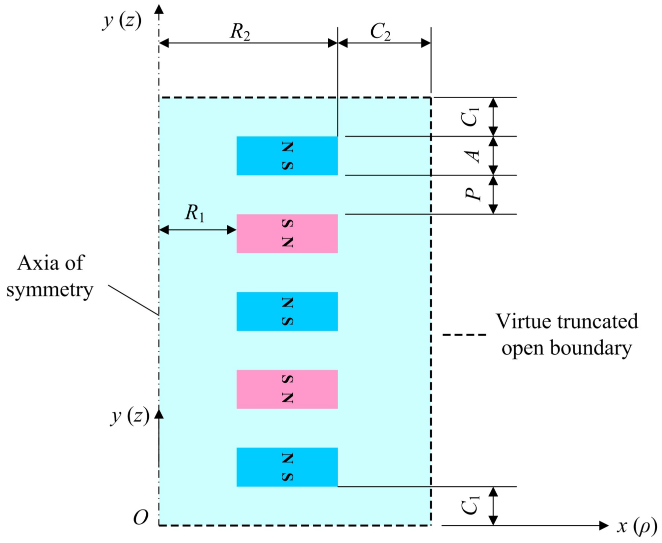

FIGURE 3. Finite-element model of the linear generator.

In Fig. 3, only PMs are included, since the coils, enclosure, rodless cylinder, and other parts are made of copper, aluminum, or nonmetallic materials, their relative permeability approximates to 1, and their influence on the field distribution is negligible. The open boundary of the model is truncated by a rectangle. In Fig. 3, C_1 and C_2 represent the distances from the truncated boundary to the periphery of PMs in the vertical and horizontal directions, respectively. R_1 and R_2 are the inner and outer radii of a magnet, respectively; A represents its thinkness; and P denotes the spacing between two neighboring magnets.

In cylindrical coordinates system, with coordinates (ρ, ϕ, z), Equation (1) can be expanded in the following form [24]

$$\frac{1}{\rho}\frac{\partial}{\partial \rho}\left(\mu_{\mathrm{r}}\rho\frac{\partial \varphi_{\mathrm{m}}}{\partial \rho}\right) + \frac{\partial}{\partial z}\left(\mu_{\mathrm{r}}\frac{\partial \varphi_{\mathrm{m}}}{\partial z}\right) = 0 \tag{2}$$

Multiply ρ at both the left and right sides of (2), we get

$$\frac{\partial}{\partial \rho}\left(\mu_{\mathrm{r}}\rho\frac{\partial \varphi_{\mathrm{m}}}{\partial \rho}\right) + \frac{\partial}{\partial z}\left(\mu_{\mathrm{r}}\rho\frac{\partial \varphi_{\mathrm{m}}}{\partial z}\right) = 0 \tag{3}$$

Let

$$x = \rho, \quad y = z, \quad \alpha = \rho\mu_{\mathrm{r}} \tag{4}$$

then Equation (3) can be transformed into the standard Laplace's equation in Cartesian coordinate system, given by

$$\frac{\partial}{\partial x}\left(\alpha\frac{\partial \varphi_{\mathrm{m}}}{\partial x}\right) + \frac{\partial}{\partial y}\left(\alpha\frac{\partial \varphi_{\mathrm{m}}}{\partial y}\right) = 0 \tag{5}$$

where α can be treated as the parameter relating with medium property. Since the permeability of permanent magnets is much larger than that of the air, the scalar magnetic potential on the permanent magnets surfaces can be regarded as equipotential. Accordingly, we can assign zero magnetic potential for reference on the south poles of magnet, namely the boundary condition is

$$\varphi_{\mathrm{m}} = 0 \qquad \text{(on the south poles of magnets)} \tag{6}$$

The scalar magnetic potential on the north pole is

$$\varphi_{\mathrm{m}} = H_{\mathrm{c}}A \qquad \text{(on the north poles of magnets)} \tag{7}$$

Here, H_{c} represents the coercive force of PMs, which is a given value. On the truncated exterior boundary, symmetric center line as well as left and right sides of each magnet, the parallel magnetic flux boundary condition, namely nature boundary condition, is assigned, and it can be written as

$$\frac{\partial \varphi_{\mathrm{m}}}{\partial n} = 0 \tag{8}$$

Partial differential Equation (5) and boundary conditions (6) to (8) constitute the boundary value problem to be solved. According to finite element method theory, this boundary value problem can be converted into the equivalent variational problem

$$\delta F(\varphi_{\mathrm{m}}) = 0 \tag{9}$$

where $F(\varphi_{\mathrm{m}})$ is the energy functional. Assuming that the model is discretized into M triangle elements, the functional can be expressed as

$$F(\varphi_{\mathrm{m}}) = \sum_{e=1}^{M} F^e(\varphi_{\mathrm{m}}^e) \tag{10}$$

where 'e' denotes the element; F^e represents the sub-functional for element 'e'; and F^e is given by following expression

$$F^e(\varphi_{\mathrm{m}}^e) = \frac{1}{2}\iint_{\Omega^e} \alpha\left[\left(\frac{\partial \varphi_{\mathrm{m}}^e}{\partial x}\right)^2 + \left(\frac{\partial \varphi_{\mathrm{m}}^e}{\partial y}\right)^2\right] \mathrm{d}\Omega \tag{11}$$

φ_{m} is a function with respect to x and y. Approximating the $\varphi_{\mathrm{m}}(x, y)$ in a triangle element using the three nodes values of $\varphi_{\mathrm{m}1}$, $\varphi_{\mathrm{m}2}$ and $\varphi_{\mathrm{m}3}$ by linear interpolation method, it can be written as

$$\varphi_{\mathrm{m}}^e(x, y) = \sum_{j=1}^{3} N_j^e(x, y)\varphi_{\mathrm{m}j}^e \tag{12}$$

where N_j^e is the interpolation function. Taking the derivatives of F^e with respect to $\varphi_{\mathrm{m}j}^e$ and written as matrix form, we can obtain

$$\left\{\frac{\partial F^e}{\partial \mathbf{\Phi}_{\mathrm{m}}^e}\right\} = [\mathbf{K}]^e \left\{\mathbf{\Phi}_{\mathrm{m}}^e\right\} \tag{13}$$

where

$$\{\mathbf{\Phi}_{\mathrm{m}}^e\} = \{\varphi_{\mathrm{m}1}^e, \varphi_{\mathrm{m}2}^e, \varphi_{\mathrm{m}3}^e\}^T; \left\{\frac{\partial F^e}{\partial \mathbf{\Phi}_{\mathrm{m}}^e}\right\} = \left\{\frac{\partial F^e}{\partial \varphi_{\mathrm{m}1}^e}, \frac{\partial F^e}{\partial \varphi_{\mathrm{m}2}^e}, \frac{\partial F^e}{\partial \varphi_{\mathrm{m}3}^e}\right\}$$

and $[\mathbf{K}]^e$ is a 3×3 elements stiffness matrix, and the value of its member is given by

$$K_{ij}^e = \frac{1}{4\triangle^e}\left(\alpha^e b_i^e b_j^e + \alpha^e c_i^e c_j^e\right) \qquad i, j = 1, 2, 3 \tag{14}$$

where b_i, b_j, c_i, and c_j are coefficients in relation to nodes coordinates, and $\triangle^e$ is the area of element 'e'.

From (4), we have

$$\alpha^e = \rho^e \mu_\mathrm{r}, \tag{15}$$

here, $\mu_\mathrm{r} = 1.0$. For triangle element 'e', ρ^e is selected as the centroid and written as

$$\rho^e = \frac{x_i + x_j + x_m}{3} \tag{16}$$

where x_i, x_j, and x_m are coordinates of x components for three nodes of element 'e', respectively, and here i, j, m are used in particular to denote the numbering of the three nodes of a triangular element.

Combining all the element stiffness matrices for M elements and applying extremum condition, we can get the following matrix equation

$$[\mathbf{K}]\{\mathbf{\Phi}_\mathrm{m}\} = 0 \tag{17}$$

where $[\mathbf{K}]$ denotes the global assembly matrix, and $\mathbf{\Phi}_\mathrm{m}$ is the vector composed of N nodes variables.

Then deal with all the boundary conditions and solve the linear system (17), thus we can obtain the scalar magnetic potentials for every nodes. Finally, using (12) we can get the magnetic field intensity H^e for any of the elements, which is expressed as follows

$$H^e = -\frac{1}{2\Delta^e}\sum_{j=1}^{3}\left(b_j^e \hat{\mathbf{a}}_x + c_j^e \hat{\mathbf{a}}_y\right)\varphi_{\mathrm{m}j}^e \tag{18}$$

where $\hat{\mathbf{a}}_x$ and $\hat{\mathbf{a}}_y$ are unit vectors.

5. NUMERICAL RESULTS

The characteristics of magnetic field distribution for the linear generator are analyzed using the proposed scalar magnetic potential finite-element method (SMPFEM).

The magnets are selected as grade N50, which are made from rare-earth Nd-Fe-B and axially magnetized, with residual magnetic flux density $B_\mathrm{r} = 1.4\,\mathrm{T}$ and coercive force $H_\mathrm{c} = 970\,\mathrm{kA/m}$. The inner and outer radii of the magnets are $R_1 = 25\,\mathrm{mm}$ and $R_2 = 50\,\mathrm{mm}$, respectively, and the thickness is $A = 15\,\mathrm{mm}$. The inner and outer radii of the coils are 55 mm and 65 mm, respectively. Therefore, the air gap between the mover and stator is $\delta = 5\,\mathrm{mm}$. The open boundary is approximated by a rectangle truncated boundary and far from the model 50 mm, namely $C_1 = C_2 = 50\,\mathrm{mm}$.

The schematic diagram of discrete model for FEM is shown in Fig. 4. The orthogonal edges of the triangular elements are 5 mm long.

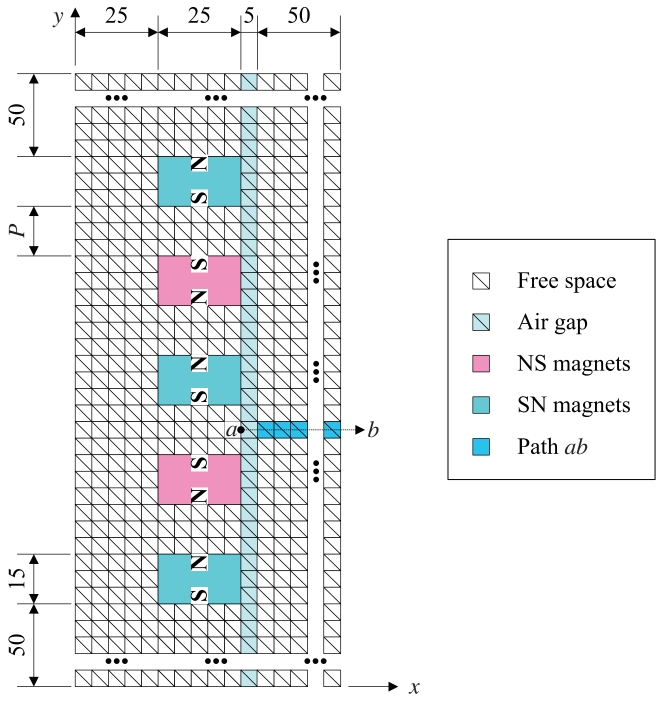

FIGURE 4. Mesh model.

5.1. Analysis of Air-Gap Magnetic Field

Here, the air-gap is defined as the clearance between the permanent magnets and coils. The air-gap is usually taken as $1 \sim 2\,\mathrm{mm}$. In this paper, considering the machining error, convenient material selection, a larger value of 5 mm is selected.

Firstly, the case of $P = A = 15\,\mathrm{mm}$ is analyzed. The calculated H_x and H_y components of the air-gap magnetic field are shown in Fig. 5 and Fig. 6, respectively.

It can be found from Fig. 5 and Fig. 6 that the distributions of H_x and H_y are approximately sinusoidal. The zero points of H_x are located in the middle of each permanent magnet, and the peaks are located in the middle of the spacing between two magnets. On the contrary, the peaks of H_y are located in the middle of each permanent magnet, and the zero points are located in the middle of the spacing between each of the two neighboring magnets.

The electromagnetic simulation software ANSYS was used to verify the obtained results, which adopts the vector magnetic potential algorithm. It can be seen that the simulated results are in good agreement with those of the proposed method except the zero or peak points of the curves, and the errors arise mainly from the rough discretization of the sample analysis for the SMPFEM method. Fig. 5 and Fig. 6 show that amplitudes of H_x and H_y are about 250 kA/m and 400 kA/m, respectively.

The contour plots of the radial and axial magnetic field distributions are shown in Fig. 7 and Fig. 8, respectively.

Fig. 7 visually shows that the radial magnetic field H_x mainly distributes in the spacers among the permanent magnets and concentrates within the range of 15 mm from the surfaces of magnets whether in the inner or external region of the ring magnets. It is obvious that the air-gap magnetic field is dominant, so a smaller air-gap is very beneficial for power generation.

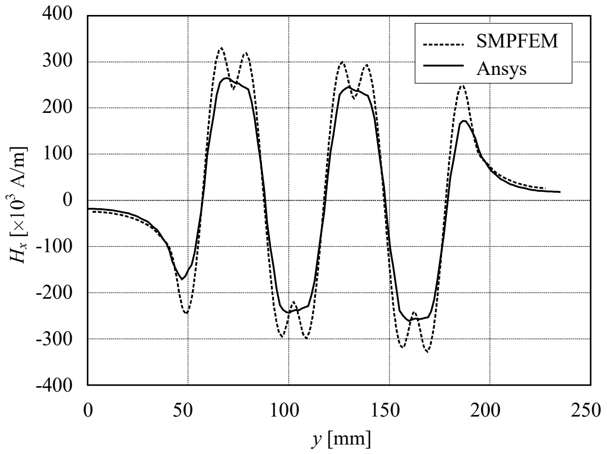

FIGURE 5. Radia component of magnetic field in air-gap for $P = 15$ mm.

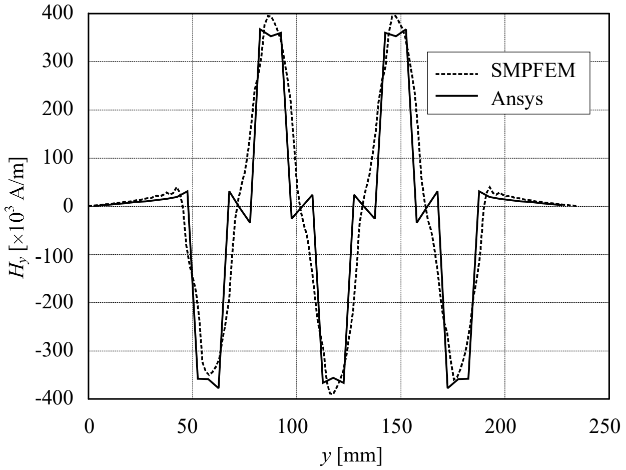

FIGURE 6. Axial component of magnetic field in air-gap for $P = 15$ mm.

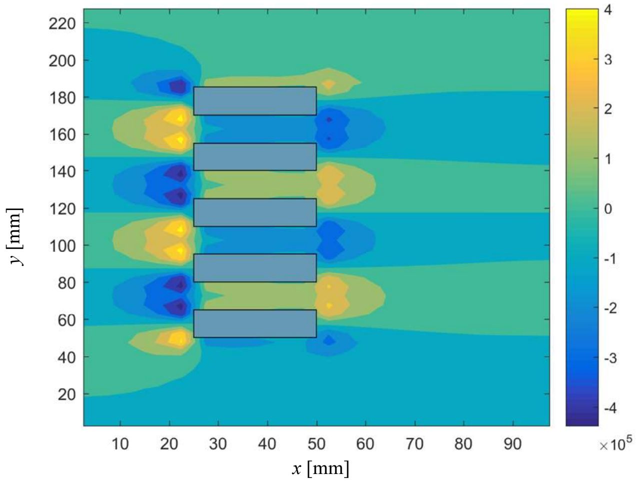

FIGURE 7. Contour plot of H_x for $P = 15$ mm.

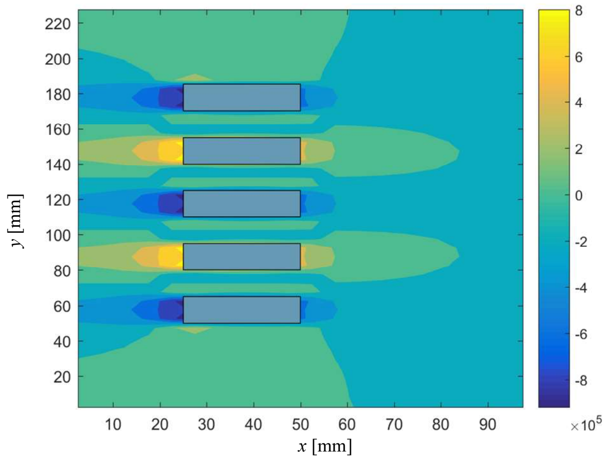

FIGURE 8. Contour plot of H_y for $P = 15$ mm.

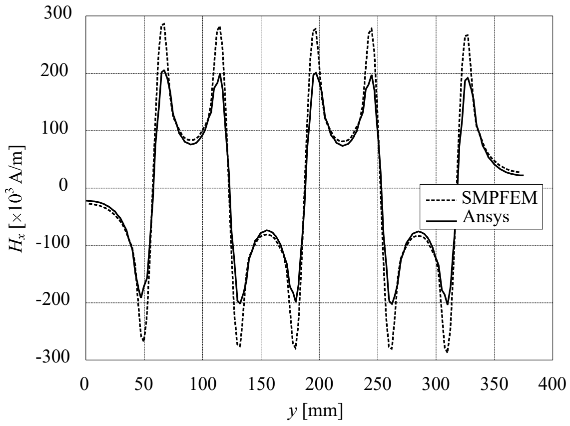

FIGURE 9. H_x in air-gap for $P = 50$ mm.

From Fig. 8, it can be found that the maximum value of the axial magnetic field H_y is about twice of that of the H_x, but it distributes in a narrow region. Along axial direction, the distribution range of H_y approximately equals the thickness of magnet, and along radial direction, H_y mainly concentrates within the range of 10 mm from the surfaces of the magnets.

Figures 7 and 8 show that the profiles of H_x and H_y are both close to a sine wave.

The advantage of taking a smaller spacing P between magnets is that the overall structure of the system is compact when the number of magnets is given, but it also brings many weaknesses; for example, the short stroke of the mover will cause frequent commutation and hence lead to serious impact and greater energy loss. The field distribution characteristics for a larger spacing of $P = 50$ mm is analyzed as follows. The calculated results for H_x and H_y are shown in Fig. 9 and Fig. 10.

As can be seen from Fig. 9, when $P = 50$ mm the wave crests of H_x become inwardly contracted, and the field strength at the center of the spacing decreases from 250 kA/m to about 90 kA/m. Fig. 10 shows that the field distribution of H_y is almost the same as that of $P = 15$ mm, i.e., it does not vary with P.

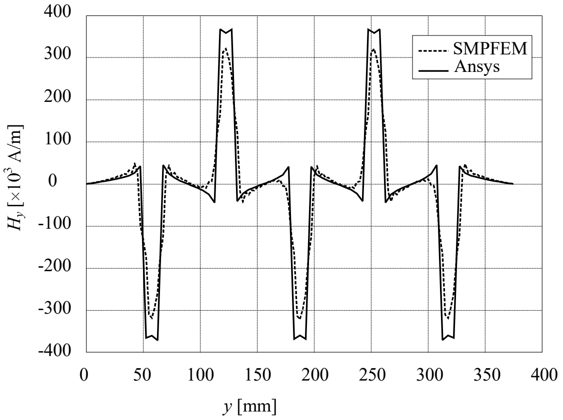

FIGURE 10. H_y in air-gap for $P = 50$ mm.

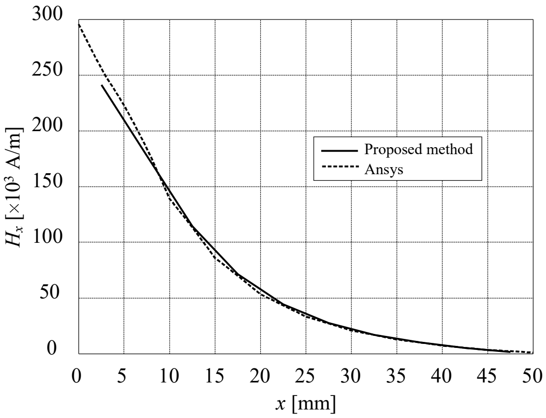

FIGURE 11. The field attenuation of permanent magnets.

In summary, when the number of magnets is fixed, a larger P will increase the stroke, which is beneficial to the acceleration of the mover, thus increasing the speed of the mover's motion, but when the P is too large it will reduce the field strength, and the field waveform will be distorted. $P = A$ should be a preferred choice, and it is better to enhance the performance of the power generation by increasing the number of magnets in the case of a fixed stroke.

5.2. The Field Attenuation of Permanent Magnet

Another issue of great concern is the attenuation of the magnetic field of permanent magnet with distance, which is in relation to the reasonable selection of the coil thickness so as to utilize as much of the magnetic field as possible.

The analyzed path is the line segment ab located at the center of spacing between magnets, as shown in Fig. 4. When $P = 15$ mm, the computed result is shown in Fig. 11. Fig. 11 shows that the field strength of permanent magnet drops rapidly and is about one-third of the maximum value when the distance from magnet is 15 mm. When the distance is 20 mm, the field strength will become about one-sixth of the maximum value. The obtained result can be used as the guidance for the coil design. When the thickness of the coil is large, the utilization of the magnetic field can be increased, but the weight increases, which will reduce the speed of the motion of the mover, as well as increase the cost, so a trade-off needs to be considered.

6. EXPERIMENT VALIDATION

A prototype of the linear generator was fabricated as shown in Fig.12. The geometric parameters of the linear generator are shown in Table 1.

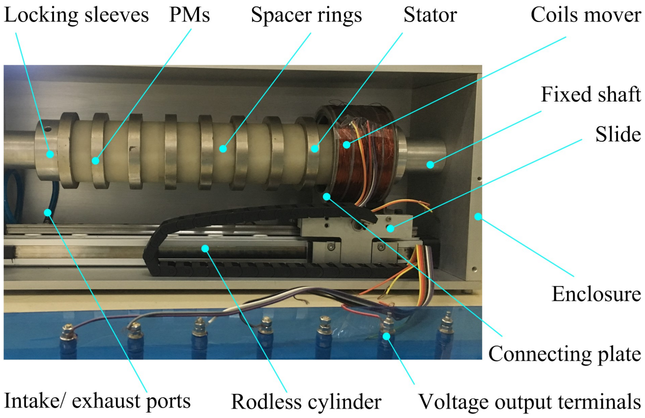

FIGURE 12. Prototype of the linear generator.

TABLE 1. Geometric parameters of the linear generator.

Items	Symbols	Values	Units
Total length	L	640	mm
Total height	H	270	mm
Total depth	W	176	mm
Cylinder stroke	S	400	mm
PM thickness	A	15	mm
Inside diameter of PM	D_1	50	mm
Outside diameter of PM	D_2	100	mm
Air-gap	g	5	mm
Inner diameter of coil	D_3	110	mm
Outer diameter of coil	D_4	130	mm
Wire specification of coil	—	24AWG	—

In the prototype, the stator is assembled by 10 pieces of permanent magnets with material NdFeB, grade N50, coercivity $H_c = 970$ kA/m, and residual magnetic induction $B_r = 1.4$ T. Permanent magnets are axially magnetized ring plates with inner diameter of $D_1 = 50$ mm, outer diameter of $D_2 = 100$ mm, thickness of $A = 15$ mm. The mover is assembled by four coils separated from each other by an acrylic plate of 3 mm thickness. The inner and outer diameters of the coil are $D_3 = 110$ mm and $D_4 = 130$ mm, respectively, and the width is designed as 8 mm. The coils are wound by insulated enameled wire of 24 AWG, with diameter about 0.5 mm. The total length of the permanent magnets and the spaces between them is equal to the cylinder stroke S, so the spacing P between neighboring magnets can be calculated to be $P = (S - 10A)/9 = 27.8$ mm.

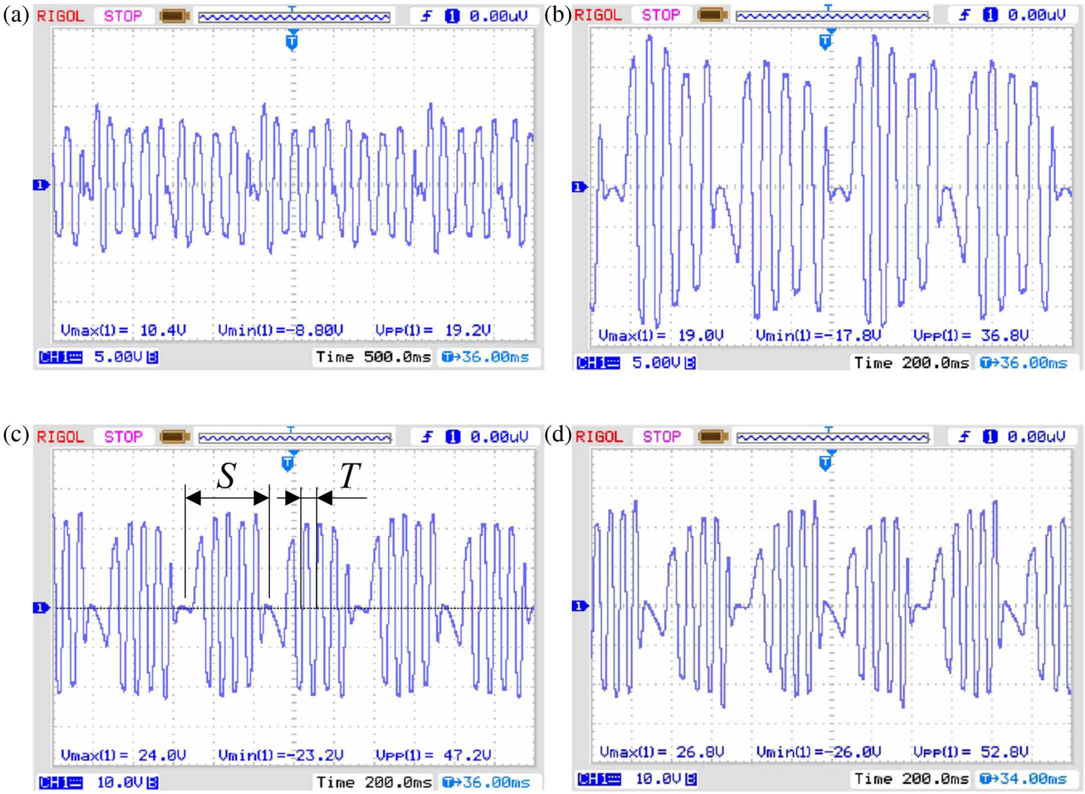

FIGURE 13. Measurement result; (a), (b), (c) and (d) are the output voltage measurement curves for different speeds of the coils mover, respectively.

By adjusting the position (opening size) of the throttle valve in the pneumatic control system, the movement speed of the mover can be changed. Fig. 13 illustrates the measured output voltage waveforms for a single coil at different operating speeds of the coils mover. Fig. 13 clearly shows that with the commutation at both ends of the stroke, the residence time of zero speed is relatively long, and there is an obvious discontinuity. Furthermore it can be found that in one cylinder stroke S there is about 5 periods of sinusoidal voltage, and due to the non-uniformity of the mover speed, there are large fluctuations in the amplitude of the output voltage. In Fig. 13, the maximum values $V_{\max}$ of the output voltage of an individual coil at different operating speeds are indicated, which are listed in Table 2. The running speed v of the mover can be obtained from the following equation

$$v = \frac{\lambda}{T} \tag{19}$$

where λ and T are the wavelength and period of one sinusoidal voltage wave, respectively, with $\lambda = 2(P + A) = 2(15 + 27.8) = 85.6\,\text{mm}$, and T can be obtained by measurement with an oscilloscope. Since the velocity of the mover is dynamically changing, the captured maximum v will differ from the real working speed v corresponding to $V_{\max}$.

Table 2 shows the maximum output voltage V_{meas} and its corresponding period and operating speed measured under different operating conditions.

The theoretical prediction of the electric potential V_{cal} can be approximated by the following equation

$$V_{\text{cal}} = B_{\text{ave}} l v \tag{20}$$

here, B_{ave} is chosen to be the average value of the field strength at the inner and outer diameters of the coil. From Fig. 11, we get $B_{\text{ave}} = (230 + 90)/2)\mu_0 = 160 \times 4 \times \pi \times 10^{-7} = 0.2\,\text{T}$. The wire length of the coil is about $l = 102\,\text{m}$. Therefore

$$V_{\text{cal}} = 0.2 \times 102 = 20.4v \tag{21}$$

The calculated values of V_{cal} for different v are shown in Table 2. It can be found that the values predicted by the theory are in reasonable agreement with the measured results. By further increasing the speed of the mover, the peak voltage output from four coils in series can exceed 100 V but with a large impact.

TABLE 2. Maximum output voltage of a single coil at different speeds.

Cases	T [ms]	v [m/s]	V_{cal}	V_{meas} [V]
1	200	0.43	8.77	10.4
2	100	0.86	17.54	19.0
3	80	1.07	21.83	24.0
4	72	1.19	24.28	25.6 V
5	66	1.30	27.74	26.8 V

7. CONCLUSION

Utilizing ocean wave energy to generate electricity is an emerging industry that has received widespread attention. In this paper, a miniaturized tubular PDLG suitable for small and medium power is proposed. This PDLG is driven by a rodless cylinder, which has the advantages of less transmission and compact structure. Only a few pneumatic components are employed to realize the automatic reciprocating motion of the coils mover. The axial and radial magnetic field distributions of the magnet assembly, namely the stator, as well as the decay characteristics of the magnetic field for the permanent magnets with distance are analyzed by the scalar magnetic potential FEM. In addition, the influence of the magnet spacing on the waveform of the field distribution is also studied. The numerical results provide valuable guidance for the selection of structural parameters of the linear generator's mover and stator. A prototype PDLG was constructed to experimentally investigate its power generation performance. The experimental results show that the voltage amplitude can reach 100 V by four series-connected coils. The experimental results are in good agreement with that of the numerical calculation.

The PDLG can operate at higher speeds, which is important for increasing power generation. In addition, the PDLG has a simple structure, is cost-effective, and is very favorable for pneumatic type energy harvesting.

Reducing impact at high speeds, the load-carrying characteristics, the increase in power generation, and the flexible converter of wave energy to pneumatic energy need to be continually researched in near future.

REFERENCES

[1] Naghavi, F., S. Sheshaprasad, M. Gardner, A. Meduri, H. Y. Kang, and H. Toliyat, "Permanent magnet linear generator design for surface riding wave energy converters," in *2021 IEEE Energy Conversion Congress and Exposition (ECCE)*, 4369–4375, Vancouver, BC, Canada, 2021.

[2] Ho, S. L., Q. Wang, S. Niu, and W. N. Fu, "A novel magnetic-geared tubular linear machine with halbach permanent-magnet arrays for tidal energy conversion," *IEEE Transactions on Magnetics*, Vol. 51, 1–4, Nov. 2015.

[3] Yamanouchi, Y., M. Tsuchiya, R. Koga, K. Yamaguchi, M. Izumi, and T. Ida, "Conceptual design of a linear power generator for undulator-type tidal current power generation," *IEEE Transactions on Applied Superconductivity*, Vol. 34, 1–5, 2024.

[4] Polinder, H., M. E. C. Damen, and F. Gardner, "Linear PM generator system for wave energy conversion in the AWS," *IEEE Transactions on Energy Conversion*, Vol. 19, 583–589, 2004.

[5] Polinder, H., M. E. C. Damen, and F. Gardner, "Design, modelling and test results of the AWS PM linear generator," *European Transactions on Electrical Power*, Vol. 15, 245–256, 2005.

[6] Polinder, H., B. C. Mecrow, A. G. Jack, P. G. Dickinson, and M. A. Mueller, "Conventional and TFPM linear generators for direct-drive wave energy conversion," *IEEE Transactions on Energy Conversion*, Vol. 20, 260–267, Jun. 2005.

[7] Seo, S.-W., K.-H. Shin, M.-M. Koo, K. Hong, I.-J. Yoon, and J.-Y. Choi, "Experimentally verifying the generation characteristics of a double-sided linear permanent magnet synchronous generator for ocean wave energy conversion," *IEEE Transactions on Applied Superconductivity*, Vol. 30, 1–4, Jun. 2020.

[8] Hodgins, N., O. Keysan, A. S. McDonald, and M. A. Mueller, "Design and testing of a linear generator for wave-energy applications," *IEEE Transactions on Industrial Electronics*, Vol. 59, 2094–2103, 2012.

[9] Baker, N. J., M. A. Mueller, and E. Spooner, "Permanent magnet air-cored tubular linear generator for marine energy converters," in *Second International Conference on Power Electronics, Machines and Drives (PEMD 2004).*, Vol. 2, 862–867, 2004.

[10] Colli, V. D., P. Cancelliere, F. Marignetti, R. D. Stefano, and M. Scarano, "A tubular-generator drive for wave energy conversion," *IEEE Transactions on Industrial Electronics*, Vol. 53, 1152–1159, Jun. 2006.

[11] Prudell, J., M. Stoddard, E. Amon, T. K. Brekken, and A. V. Jouanne, "A permanent-magnet tubular linear generator for ocean wave energy conversion," *IEEE Transactions on Industry Applications*, Vol. 46, 2392–2400, Nov. 2010.

[12] Nie, Z., X. Xiao, R. McMahon, P. Clifton, Y. Wu, and S. Shao, "Emulation and control methods for direct drive linear wave energy converters," *IEEE Transactions on Industrial Informatics*, Vol. 9, 790–798, 2013.

[13] Jing, H., N. Maki, T. Ida, and M. Izumi, "Performance comparison of mw class tubular linear generators for wave energy conversion," *Journal Title*, Vol. 27, 1–6, Sept. 2017.

[14] Chen, H., S. Zhao, H. Wang, and R. Nie, "A novel single-phase tubular permanent magnet linear generator," *Journal Title*, Vol. 30, 1–5, Jun. 2020.

[15] Chen, M., L. Huang, M. Hu, B. Hu, and G. Ahmad, "A spiral translator permanent magnet transverse flux linear generator used in direct-drive wave energy converter," *IEEE Transactions on Magnetics*, Vol. 57, 1–5, Jul. 2021.

[16] Qiu, S., W. Zhao, C. Zhang, J. K. H. Shek, and H. Wang, "A novel structure of tubular staggered transverse-flux permanent-magnet linear generator for wave energy conversion," *IEEE Transactions on Energy Conversion*, Vol. 37, 24–35, Mar. 2022.

[17] Huang, L., J. Liu, H. Yu, R. Qu, H. Chen, and H. Fang, "Winding configuration and performance investigations of a tubular superconducting flux-switching linear generator," *IEEE Transactions on Applied Superconductivity*, Vol. 25, 1–5, 2015.

[18] Farrok, O., M. R. Islam, K. M. Muttaqi, D. Sutanto, and J. Zhu, "Design and optimization of a novel dual-port linear generator for oceanic wave energy conversion," *IEEE Transactions on Industrial Electronics*, Vol. 67, 3409–3418, May 2020.

[19] Virtic, P., P. Pisek, T. Marcic, M. Hadziselimovic, and B. Stumberger, "Analytical analysis of magnetic field and back electromotive force calculation of an axial-flux permanent magnet synchronous generator with coreless stator," *Journal Title*, Vol. 44, 4333–4336, Nov. 2008.

[20] Musolino, A., M. Raugi, R. Rizzo, and L. Sani, "A semi-anaytical model for the analysis of a permanent magnet tubular linear generator," *Journal Title*, Vol. 54, 204–212, 2018.

[21] Kim, J.-M., J.-Y. Choi, M.-M. Koo, H.-J. Shin, and S.-H. Lee, "Characteristic analysis of tubular-type permanent-magnet linear magnetic coupling based on analytical magnetic field calculations," *Journal Title*, Vol. 26, 1–5, Jun. 2016.

[22] Alhamadi, M. A., R. Wang, and N. A. Demerdash, "Vector potential 3d-finite element modeling of magnetic fields in permanent magnet devices," *IEEE Transactions on Magnetics*, Vol. 27, 5016 –5018, Nov. 1991.

[23] Hayt, W. and J. Buck, *Engineering Electromagnetics*, The Mcgraw-Hill Companies, Inc., 2012.

[24] Jin, J., *The Finite Element Method in Electromagnetics*, Wiley-IEEE Press, 2002.